

Supplement to Codimensional Incremental Potential Contact

MINCHEN LI, University of California, Los Angeles & University of Pennsylvania & Adobe Research

DANNY M. KAUFMAN, Adobe Research

CHENFANFU JIANG, University of California, Los Angeles & University of Pennsylvania

CCS Concepts: • Computing methodologies → Physical simulation.

Additional Key Words and Phrases: Strain Limiting, Contact Mechanics, Mixed-Dimensional Elastodynamics, Constrained Optimization

ACM Reference Format:

Minchen Li, Danny M. Kaufman, and Chenfanfu Jiang. 2021. Supplement to Codimensional Incremental Potential Contact. *ACM Trans. Graph.* 40, 4, Article 170 (August 2021), 5 pages. <https://doi.org/10.1145/3450626.3459767>

CONTENTS

Contents	1
1 Volumetric Shell v.s. Discrete Shell	1
2 Membrane Locking w.r.t. Resolution and Bending Stiffness	1
3 Isotropic Strain Limiting Derivative Derivations	2
4 Anisotropic Strain Limiting Derivations	3
4.1 Quadratically Approximating Data-Driven Model	3
4.2 Implementation Details	3
5 Robust and Efficient Implementation of IPC Friction	3
6 Friction Validation on Cloth	4
7 Termination Criteria	4
8 Rod Bending Modulus	4
9 Shell Energies	4
References	5

1 VOLUMETRIC SHELL V.S. DISCRETE SHELL

Linear volumetric elements could be used as an alternative to simulate thin materials with geometric thickness. However, as their bending is realized by shearing deformation, a shearing penalty serves as an extra source of bending stiffness, making their bending behavior artificially stiffened.

Here we use the cylindrical cloth twisting example to demonstrate this artifact in a side-by-side comparison between the codimensional twist, simulated with C-IPC a volumetric twist simulated

Authors' addresses: Minchen Li, University of California, Los Angeles & University of Pennsylvania & Adobe Research, minchernl@gmail.com; Danny M. Kaufman, Adobe Research, danny.kaufman.cs@gmail.com; Chenfanfu Jiang, University of California, Los Angeles & University of Pennsylvania, chenfanfu.jiang@gmail.com.

Permission to make digital or hard copies of all or part of this work for personal or classroom use is granted without fee provided that copies are not made or distributed for profit or commercial advantage and that copies bear this notice and the full citation on the first page. Copyrights for components of this work owned by others than ACM must be honored. Abstracting with credit is permitted. To copy otherwise, or republish, to post on servers or to redistribute to lists, requires prior specific permission and/or a fee. Request permissions from permissions@acm.org.

© 2021 Association for Computing Machinery.

0730-0301/2021/8-ART170 \$15.00

<https://doi.org/10.1145/3450626.3459767>

by IPC [Li et al. 2020]. Following IPC we generate a volumetric mesh by extruding the codimensional cylinder surface (87.6K nodes) in both outward and inward radial directions and then sealing the circular gaps on the two sides with a single layer of triangles to create a closed volumetric cylinder shell mesh. We then apply Tetgen [Si 2015] to tetrahedralize this volume (without additional Steiner points) resulting in a 175.2K-node tetrahedral mesh. Here extrusion distances are both 0.75mm, making the thickness of the volumetric shell 1.5mm, to match the contact offset ζ used in our codimensional version. However, as thickness values used to compute volume integrals for mass and elasticity in the codimensional version utilize a cotton material (0.318mm), we apply the same Poisson's ratio but set the density and Young's modulus in the volumetric version to $0.318/1.5 = 0.212 \times$ that of the codimensional version to unify material properties and so make the two models comparable.

Applying identical boundary conditions, the volumetric simulation clearly obtains artificially stiffened bending, with smoother and less frequent wrinkles, and noticeable gaps between the touching layers. See Figure 1, top for the volumetric results and bottom for the comparable C-IPC version. As there are 2 \times as many nodal DOF in the volumetric model than in C-IPC, the volumetric simulation is also, likewise, more expensive. For the first 200 time steps, the C-IPC simulation, per time step took 1.7min and 9.5 iterations on average, while the volumetric IPC simulation took 3.4min and 13.1 iterations. In addition, we observe that our C-IPC simulation also generates more contact pairs to process (848K at max) per time step than the volumetric simulation (474K at max) due to the finer wrinkling behavior obtained.

2 MEMBRANE LOCKING W.R.T. RESOLUTION AND BENDING STIFFNESS

As discussed in our introduction, increasing resolution can alleviate membrane locking. However, shell models can continue to suffer severe numerical stiffening in bending modes as we vary cloth materials even, as we show here, at high resolution.

To investigate resolution dependence in membrane locking, we test the cloth drape on the static sphere with mesh resolutions varying from 8K up to 246K nodes. We first simulate these drapes with the default 1 \times (reported cotton) membrane stiffness *without* strain limiting. In Figure 2 we see that, for this material, as resolution increases, membrane-locking artifacts becomes less and less severe. Specifically, at higher resolutions with 85K and 246K nodes, locking artifacts are negligible except for sharp turns on some wrinkle profiles.

However, the severity of membrane locking behaviors vary with both resolution *and* material. Here, membrane locking is essentially an artificial stiffening of bending by an additional bending penalty sourced from the membrane energy. If (as in the above example) the



Fig. 1. Volumetric Shell v.s. Discrete Shell. From left to right, we compare the 5th, 100th, and 200th time step result between a volumetric version (top) and our codimensional version (bottom) of the cylinder cloth twisting example with the same material properties and boundary conditions. The smoother and lower frequency wrinkles, and the larger gaps between the touching layers in the volumetric results clearly demonstrate the artificially stiffened bending behavior.

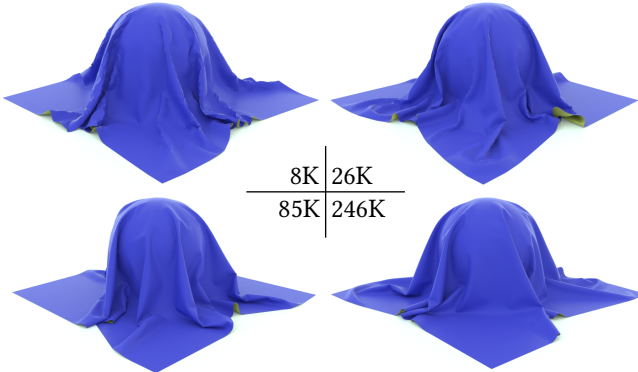


Fig. 2. Membrane Locking w.r.t. Resolution. As resolution increases, here membrane locking-artifacts in the cloth on sphere example, simulated using $1\times$ the smallest membrane stiffness *without strain limiting*, becomes less severe and eventually nearly negligible at 85K nodes and 246K nodes, except for sharp turns on some of the wrinkle profiles.

original bending to be modeled is already large, membrane locking artifacts can more easily be reduced with increased resolution. On the other hand, if we simulate the same example set up as above, except now with a $0.01\times$ bending stiffness (as applied in Figure 6, bottom of our primary text), increasing resolution is not nearly as helpful. For example, now even at a 246K node resolution, we still see obvious membrane-locking artifacts; see Figure 3, left and compare with C-IPC's strain-limited result in Figure 3, right.

3 ISOTROPIC STRAIN LIMITING DERIVATIVE DERIVATIONS

We require derivatives of the singular value decomposition (SVD):

$$\frac{\partial S_{ii}}{\partial F} = u_i v_i^T, \quad \frac{\partial^2 S_{ii}}{\partial F^2} = \frac{\partial(u_i v_i^T)}{\partial F} = \frac{\partial u_i}{\partial F} v_i^T + u_i \frac{\partial v_i}{\partial F}^T \quad (1)$$

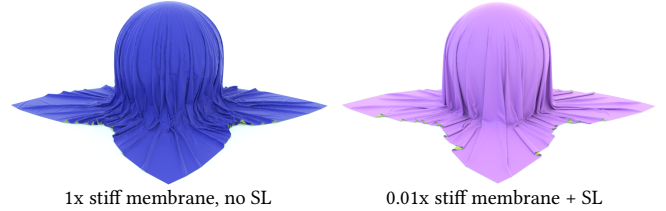


Fig. 3. Membrane Locking under Small Bending. With $0.01\times$ bending stiffness, membrane-locking artifacts remain severe even at a resolution of 246K nodes when simulated with $1\times$ the smallest membrane stiffness *without strain limiting* (left). Compare to our C-IPC result with strain limiting (right).

where $\frac{\partial u_i}{\partial F}$ and $\frac{\partial v_i}{\partial F}$ can be found in Xu et al. [2015].

Then if we denote the barrier $b_{t,i}$ for i -th singular value of triangle t , we have

$$\begin{aligned} \frac{\partial b_{t,i}}{\partial x} &= \frac{\partial b_{t,i}}{\partial S_{t,ii}} \frac{\partial S_{t,ii}}{\partial F_t} \frac{\partial F_t}{\partial x} \\ \frac{\partial^2 b_{t,i}}{\partial x^2} &= \frac{\partial S_{t,ii}}{\partial x} \frac{\partial^2 b_{t,i}}{\partial S_{t,ii}^2} \frac{\partial S_{t,ii}}{\partial x} + \frac{\partial b_{t,i}}{\partial S_{t,ii}} \frac{\partial^2 S_{t,ii}}{\partial x^2} \end{aligned} \quad (2)$$

where $\frac{\partial F_t}{\partial x}$ can be found in anisotropic strain limiting implementation detail section.

For the barrier derivatives, we have

$$\begin{aligned} \frac{\partial b_{t,i}}{\partial S_{t,ii}} &= \frac{\kappa_s}{(s - \hat{s})^2} (2(\hat{s} - S_{t,ii}) \ln(\frac{s - S_{t,ii}}{s - \hat{s}}) + \frac{(\hat{s} - S_{t,ii})^2}{s - S_{t,ii}}) \\ \frac{\partial^2 b_{t,i}}{\partial S_{t,ii}^2} &= \frac{\kappa_s}{(s - \hat{s})^2} (-2 \ln(\frac{s - S_{t,ii}}{s - \hat{s}}) - 4 \frac{\hat{s} - S_{t,ii}}{s - S_{t,ii}} + (\frac{\hat{s} - S_{t,ii}}{s - S_{t,ii}})^2) \end{aligned} \quad (3)$$

then together with

$$\frac{\partial S_{t,ii}}{\partial x} = \frac{\partial S_{t,ii}}{\partial F_t} \frac{\partial F_t}{\partial x} \quad \text{and} \quad \frac{\partial^2 S_{t,ii}}{\partial x^2} = \frac{\partial F_t}{\partial x} \frac{\partial^2 S_{t,ii}}{\partial F_t^2} \frac{\partial F_t}{\partial x}, \quad (4)$$

we can efficiently compute

$$\begin{aligned}\frac{\partial b_t}{\partial x} &= \sum_i \left(\frac{\partial b_{t,i}}{\partial S_{t,ii}} \frac{\partial S_{t,ii}}{\partial F_t} \right) \frac{\partial F_t}{\partial x}, \\ \frac{\partial^2 b_{t,i}}{\partial x^2} &= \frac{\partial F_t}{\partial x}^T \sum_i \left(\frac{\partial^2 b_{t,i}}{\partial F_t^2} \right) \frac{\partial F_t}{\partial x}\end{aligned}\quad (5)$$

where $\frac{\partial^2 b_{t,i}}{\partial F_t^2} = \frac{\partial S_{t,ii}}{\partial F_t}^T \frac{\partial^2 b_{t,i}}{\partial S_{t,ii}^2} \frac{\partial S_{t,ii}}{\partial F_t} + \frac{\partial b_{t,i}}{\partial S_{t,ii}} \frac{\partial^2 S_{t,ii}}{\partial F_t^2}$.

For SPD projection we can then process the 6x6 matrix $\sum_i (\frac{\partial^2 b_{t,i}}{\partial F_t^2})$.

4 ANISOTROPIC STRAIN LIMITING DERIVATIONS

4.1 Quadratically Approximating Data-Driven Model

The 1st-order derivatives of ψ can be computed as

$$\begin{aligned}\frac{\partial \psi}{\partial \tilde{E}_{11}} &= a_{11} \eta'_1(\tilde{E}_{11}^2) \tilde{E}_{11} + a_{12} \eta'_2(\tilde{E}_{11} \tilde{E}_{22}) \tilde{E}_{22}, \\ \frac{\partial \psi}{\partial \tilde{E}_{22}} &= a_{22} \eta'_3(\tilde{E}_{22}^2) \tilde{E}_{22} + a_{12} \eta'_2(\tilde{E}_{11} \tilde{E}_{22}) \tilde{E}_{11}, \\ \frac{\partial \psi}{\partial \tilde{E}_{12}} &= 2G_{12} \eta'_4(\tilde{E}_{12}^2) \tilde{E}_{12}.\end{aligned}\quad (6)$$

When $\tilde{E} = 0$ the element is in rest shape, and all gradients above are equal to 0.

For the 2nd-order derivatives we have

$$\begin{aligned}\frac{\partial^2 \psi}{\partial \tilde{E}_{11}^2} &= 2a_{11} \eta''_1(\tilde{E}_{11}^2) \tilde{E}_{11} + a_{11} \eta'_1(\tilde{E}_{11}^2) + a_{12} \eta''_2(\tilde{E}_{11} \tilde{E}_{22}) \tilde{E}_{22}^2, \\ \frac{\partial^2 \psi}{\partial \tilde{E}_{11} \partial \tilde{E}_{22}} &= \frac{\partial^2 \psi}{\partial \tilde{E}_{22} \partial \tilde{E}_{11}} = a_{12} \eta''_2(\tilde{E}_{11} \tilde{E}_{22}) \tilde{E}_{22} \tilde{E}_{11} + a_{12} \eta'_2(\tilde{E}_{11} \tilde{E}_{22}), \\ \frac{\partial^2 \psi}{\partial \tilde{E}_{22}^2} &= 2a_{22} \eta''_3(\tilde{E}_{22}^2) \tilde{E}_{22}^2 + a_{22} \eta'_3(\tilde{E}_{22}^2) + a_{12} \eta''_2(\tilde{E}_{11} \tilde{E}_{22}) \tilde{E}_{11}^2, \\ \frac{\partial^2 \psi}{\partial \tilde{E}_{12}^2} &= 4G_{12} \eta''_4(\tilde{E}_{12}^2) \tilde{E}_{12}^2 + 2G_{12} \eta'_4(\tilde{E}_{12}^2),\end{aligned}\quad (7)$$

and all other terms are 0. When $\tilde{E} = 0$, we have

$$\begin{aligned}\frac{\partial^2 \psi}{\partial \tilde{E}_{11}^2} &= a_{11}, \quad \frac{\partial^2 \psi}{\partial \tilde{E}_{22}^2} = a_{22}, \quad \frac{\partial^2 \psi}{\partial \tilde{E}_{12}^2} = 2G_{12}, \\ \frac{\partial^2 \psi}{\partial \tilde{E}_{11} \partial \tilde{E}_{22}} &= \frac{\partial^2 \psi}{\partial \tilde{E}_{22} \partial \tilde{E}_{11}} = a_{12},\end{aligned}\quad (8)$$

all constants. Thus to quadratically approximate the data-driven model at $\tilde{E} = 0$, using our barrier model, we just simply need to use the same stiffnesses.

4.2 Implementation Details

For simplicity, if we align the cloth weft and warp directions to the coordinate axes, we can easily compute \tilde{E} from the 3x2 deformation gradient $F = [x_2 - x_1, x_3 - x_1][X'_2 - X'_1, X'_3 - X'_1]^{-1}$ as

$$\tilde{E}_{ij} = \frac{1}{2}(F_{mi}F_{mj} - \delta_{ij}),$$

so we have

$$\begin{aligned}\frac{\partial \tilde{E}_{ij}}{\partial F_{kl}} &= \frac{1}{2}(\delta_{il}F_{kj} + F_{ki}\delta_{jl}), \\ \frac{\partial^2 \tilde{E}_{ij}}{\partial F_{kl} \partial F_{mn}} &= \frac{1}{2}\delta_{mk}(\delta_{il}\delta_{nj} + \delta_{ni}\delta_{jl}).\end{aligned}\quad (9)$$

Then together with $\partial \psi$ above and $dF/dx = \begin{bmatrix} -I \\ -I \end{bmatrix} \begin{bmatrix} I \\ 0 \end{bmatrix} \begin{bmatrix} 0 \\ I \end{bmatrix}$: B , with $B = [X'_2 - X'_1, X'_3 - X'_1]^{-1}$ we have

$$\frac{dF}{dx} = \begin{bmatrix} -(B_{11} + B_{21}) & * & B_{11} & * & B_{21} & * \\ * & * & B_{12} & * & B_{22} & * \\ -(B_{12} + B_{22}) & * & * & * & * & * \end{bmatrix}, \quad (10)$$

with * indicating repetition of the top-left entry. We are then able to implement the constitutive model via

$$\frac{\partial \psi}{\partial x} = \frac{\partial \psi}{\partial \tilde{E}} \frac{\partial \tilde{E}}{\partial F} \frac{\partial F}{\partial x} \quad \text{and} \quad \frac{\partial^2 \psi}{\partial x^2} = \left(\frac{\partial \psi}{\partial F} \right)^T \frac{\partial^2 \psi}{\partial F^2} \frac{\partial F}{\partial x} \quad (11)$$

where

$$\frac{\partial^2 \psi}{\partial F^2} = \left(\frac{\partial \tilde{E}}{\partial F} \right)^T \frac{\partial^2 \psi}{\partial \tilde{E}^2} \frac{\partial \tilde{E}}{\partial F} + \frac{\partial \psi}{\partial \tilde{E}} \frac{\partial^2 \tilde{E}}{\partial F^2}.$$

5 ROBUST AND EFFICIENT IMPLEMENTATION OF IPC FRICTION

Computing the IPC friction potential, f_0 is well defined without division by 0.

Friction gradient/force computation requires a robust implementation that uses algebraically derived $\frac{f_1(||u_k||)}{||u_k||}$, which does not contain division by 0 in construction of f_1 .

For the friction Hessian, the inner 2×2 matrix is

$$\frac{f'_1(||u_k||)||u_k|| - f_1(||u_k||)}{||u_k||^3} u_k u_k^T + \frac{f_1(||u_k||)}{||u_k||} I_2.$$

Here we need to first algebraically derive $\frac{f'_1(||u_k||)||u_k|| - f_1(||u_k||)}{||u_k||^2}$ which does not contain division by 0, by construction, and note that $\frac{u_k u_k^T}{||u_k||}$ is always bounded and equals 0 when $||u_k|| = 0$, in which case, since $\frac{f_1(||u_k||)}{||u_k||} > 0$ always holds, there is no need for SPD projection.

Let $u_k = (x, y)$,

$$\begin{aligned}&\frac{f'_1(||u_k||)||u_k|| - f_1(||u_k||)}{||u_k||^3} u_k u_k^T + \frac{f_1(||u_k||)}{||u_k||} I_2 \\ &= \frac{f'_1(||u_k||)}{||u_k||^2} u_k u_k^T + \frac{-f_1(||u_k||)}{||u_k||^3} \begin{bmatrix} x^2 & xy \\ xy & y^2 \end{bmatrix} \\ &\quad + \frac{f_1(||u_k||)}{||u_k||^3} \begin{bmatrix} x^2 + y^2 & 0 \\ 0 & x^2 + y^2 \end{bmatrix} \\ &= \frac{f'_1(||u_k||)}{||u_k||^2} u_k u_k^T + \frac{f_1(||u_k||)}{||u_k||^3} \begin{bmatrix} y^2 & -xy \\ -xy & x^2 \end{bmatrix} \\ &= \frac{f'_1(||u_k||)}{||u_k||^2} u_k u_k^T + \frac{f_1(||u_k||)}{||u_k||^3} \bar{u}_k \bar{u}_k^T\end{aligned}\quad (12)$$

where $\bar{u}_k = (-y, x)$. So for $\|u_k\| \geq \epsilon_v h$ when we have $f'_1(\cdot) = 0$ and $f_1(\cdot) = 1$, the matrix is always SPD (we must compute using \bar{u}_k as the original formula can still be not SPD due to numerical error of subtraction); otherwise we project the 2x2 matrix.

6 FRICTION VALIDATION ON CLOTH

We confirm that C-IPC inherits the same accurate friction modeling behavior from IPC. We place a 0.5m-wide piece of square cloth (8K nodes) on a 26.565°-inclined slope (critical friction coefficient equals 0.5), and simulate it for 4s to test stick-slip behavior. For each time step we iteratively update the normal forces λ and the tangent operators T until convergence to a fully implicit solution. Here, even with our default parameter settings ($\hat{d} = 10^{-3} m$, $\epsilon_v = 10^{-3} m/s$, $h = 0.04s$), C-IPC obtains stiction with the critical friction coefficient $\mu = 0.5$, and obtains sliding even at $\mu = 0.49$ (99.8% of the critical coefficient), and so well-matches real-world behavior.

7 TERMINATION CRITERIA

Following IPC [Li et al. 2020], we set Newton iteration stopping tolerance ϵ_d on the Newton increment (search direction p) divided by time step size h . This has unit of velocity (m/s). Monitoring the scaled Newton increment helps to conveniently generalize convergence across complex scenes containing objects with drastically differing density, dimension, and stiffness scales. However, we observe that the residual-iteration curve when directly using infinity norm [Li et al. 2020] of the scaled Newton increment is non-smooth and oscillatory (although with an appropriately diminishing trend). This makes it nontrivial to be used for early termination as especially used in graphics applications. Therefore, in C-IPC we apply a normalized L^2 norm of the scaled Newton increment as the residual measurement:

$$r = \frac{1}{h} \sqrt{\frac{\|p\|^2}{(n - n_k)^2}} \quad (13)$$

where n is the total number of nodes in the scene and n_k is the number of kinematic nodes. Here r still maintains units of velocity as a measurement for convergence but with a much smoother residual-iteration curve. In addition, we require a sequence of l iterations all satisfying $r < \epsilon_d$ to terminate the optimization to further facilitate a robust early termination strategy.

In our experiments we use default $l = 3$ and $\epsilon_d = 10^{-3} m/s$ for all examples, except for card shuffling where we apply $\epsilon_d = 5 \times 10^{-4} m/s$ to capture the intricate dynamics.

8 ROD BENDING MODULUS

In discrete rods model [Bergou et al. 2008], the bending energy is directly integrated over the length of the rod as

$$E_{\text{bend}}(x) = \sum_{i=1}^n \frac{\alpha(\kappa b_i)^2}{\bar{l}_i} \quad (14)$$

Here κb_i is the curvature binormal at a vertex, $\bar{l}_i = |\bar{e}^{i-1}| + |\bar{e}^i|$ where $|\bar{e}^i|$ is the rest length of edge i , and α is an adjustable parameter to control the stiffness of bending. As we know when a rod becomes thicker, it is harder to bend, which means we need to manually increase α accordingly and this makes setting up examples inconvenient.

According to Kirchoff rod theory [Dill 1992], the bending energy of rod at a unit length is defined as

$$\frac{1}{2} Er^4 \frac{\pi}{4} \kappa^2$$

where E is the bending modulus in Pa unit, r is the radius of the rod, and $\kappa = \frac{\kappa b}{\bar{l}/2}$ is the point-wise curvature [Bergou et al. 2008]. Integrating this quantity over rod length then gives us

$$\begin{aligned} E_{\text{bend}}(x) &= \int_{\Omega} \frac{1}{2} Er^4 \frac{\pi}{4} \kappa^2 dl \\ &\approx \sum_i \frac{\bar{l}_i}{2} \frac{1}{2} Er^4 \frac{\pi}{4} \left(\frac{\kappa b_i}{\bar{l}_i/2} \right)^2 \\ &= \sum_i Er^4 \frac{\pi}{4} \frac{(\kappa b_i)^2}{\bar{l}_i} \end{aligned} \quad (15)$$

Combining with Equation 14 we obtain that the α in Bergou et al. [2008] is associated with the rod's radius as

$$\alpha = Er^4 \frac{\pi}{4}$$

so now the change of rod thickness under a certain bending modulus E can be automatically reflected in the bending stiffness. This enables us to easily setup rod examples starting from real material thickness and Young's modulus of e.g. hair, iron, etc, without tuning bending stiffness α . A more general form can be found in Section 4 of Bergou et al. [2010].

9 SHELL ENERGIES

Finally we elaborate on how our shell energies are integrated so that thickness changes are also directly included in *elasticity* behavior with Young's modulus E and Poisson's ratio ν directly used to set stiffnesses.

Membrane Energy. We apply the membrane energy in Koiter's shell model from Chen et al. [2018]:

$$\Psi_{\text{ShellM}}(x) = \sum_t V_t \frac{1}{4} \left(\frac{1}{2} \lambda \text{tr}^2(M_t) + \mu \text{tr}(M_t^2) \right); \quad (16)$$

where $M_t = \bar{F}_t^{-1} F_t - I$, with F_t and \bar{F}_t the first fundamental form of triangle t in world space and material space respectively, μ and λ are the Lamé parameters for shells, and $V_t = |\bar{t}| \xi_t$ is the volume weighting with triangle rest area, $|\bar{t}|$, and thickness, ξ_t .

Bending Energy. We apply the discrete shell (hinge) bending energy from Grinspun et al. [2003]:

$$\Psi_{\text{ShellB}}(x) = \sum_e k_e (\theta_e - \bar{\theta}_e)^2 \|\bar{e}\| / \bar{h}_e \quad (17)$$

where k_e is the bending stiffness, θ_e and $\bar{\theta}_e$ are the dihedral angles of edge e in world space and material space respectively, $\|\bar{e}\|$ is the rest length of edge e , and \bar{h}_e is $\frac{1}{3} \times$ of the average of the heights of the two triangles incident to the edge e [Grinspun et al. 2003]. Here we apply the parameterization in Tamstorf and Grinspun [2013]

$$k_e = \frac{E}{24(1-\nu^2)} \xi_e^3, \quad (18)$$

setting the bending stiffness k_e to half of the flexural rigidity so that it is automatically adjusted with the thickness ξ_e , and we can

instead intuitively set the Young's modulus E and Poisson's ratio ν according to measured cloth material parameters [Penava et al. 2014].

Material Settings. In Penava et al. [2014], we find densities, Young's moduli, and Poisson's ratios for a range of cloth materials. As most cloth are anisotropic, the Young's moduli and Poisson's ratios vary with directions (see [Penava et al. 2014], Table 3). Therefore, we pick the smallest Young's modulus and Poisson's ratio among all directions per material to perform our experiments. For example, from Penava et al. [2014], Table 3, we see cotton has the smallest Young's modulus 0.821MPa in 45° , and the smallest Poisson's ratio 0.243 at 90° . However, as discussed in our main text, despite applying this smallest measured stiffness value we still observe membrane locking at moderate simulation resolutions. Instead C-IPC applies a smaller scaled ($0.1\times$ or even $0.01\times$ the smallest measured value) Young's modulus to avoid membrane locking *combined* with constitutive strain-limiting barrier to ensure no stretching artifacts. Our applied strain limits are set based on Penava et al. [2014], Table 2, where the measured strain range reflects the elasticity range. For example, cotton's largest measured strain range is 6.08% at 30° , and we use this value to set its strain limit. Applying C-IPC to accurately model the anisotropic properties of cloth to closely match measurements, and

likewise to properly handle plastic deformation and cloth fracture all remain interesting future work.

REFERENCES

- Miklós Bergou, Basile Audoly, Etienne Vouga, Max Wardetzky, and Eitan Grinspun. 2010. Discrete viscous threads. *ACM Transactions on graphics (TOG)* 29, 4 (2010), 1–10.
- Miklós Bergou, Max Wardetzky, Stephen Robinson, Basile Audoly, and Eitan Grinspun. 2008. Discrete elastic rods. In *ACM SIGGRAPH 2008 papers*. 1–12.
- Hsiao-Yu Chen, Arnav Sastry, Wim M van Rees, and Etienne Vouga. 2018. Physical simulation of environmentally induced thin shell deformation. *ACM Transactions on Graphics (TOG)* 37, 4 (2018), 1–13.
- Ellis Harold Dill. 1992. Kirchhoff's theory of rods. *Archive for History of Exact Sciences* 44, 1 (1992), 1–23.
- Eitan Grinspun, Anil N Hirani, Mathieu Desbrun, and Peter Schröder. 2003. Discrete shells. In *Proceedings of the 2003 ACM SIGGRAPH/Eurographics symposium on Computer animation*. Citeseer, 62–67.
- Minchen Li, Zachary Ferguson, Teseo Schneider, Timothy Langlois, Denis Zorin, Daniele Panozzo, Chenfanfu Jiang, and Danny M. Kaufman. 2020. Incremental Potential Contact: Intersection- and Inversion-free Large Deformation Dynamics. *ACM Transactions on Graphics* 39, 4 (2020).
- Željko Penava, Diana Šimić-Penava, and Ž Knežić. 2014. Determination of the elastic constants of plain woven fabrics by a tensile test in various directions. *Fibres & Textiles in Eastern Europe* (2014).
- Hang Si. 2015. TetGen, a Delaunay-based quality tetrahedral mesh generator. *ACM Transactions on Mathematical Software (TOMS)* 41, 2 (2015), 1–36.
- Rasmus Tamstorf and Eitan Grinspun. 2013. Discrete bending forces and their Jacobians. *Graphical models* 75, 6 (2013), 362–370.
- Hongyi Xu, Funshing Sin, Yufeng Zhu, and Jernej Barbič. 2015. Nonlinear material design using principal stretches. *ACM Transactions on Graphics (TOG)* 34, 4 (2015), 1–11.